Representative structural element approach for assessing the mechanical properties of automated fibre placement-induced defects

Andreas Friedel [a],[*], Sebastian Heimbs [b], Peter Horst [b], Carsten Schmidt [c], Marc Timmermann [c]

[a] *Institute of Aircraft Design and Lightweight Structures, Technische Universität Braunschweig, Ottenbecker Damm 12, Stade, Germany*
[b] *Institute of Aircraft Design and Lightweight Structures, Technische Universität Braunschweig, Hermann-Blenk-Straße 35, Braunschweig, Germany*
[c] *Institute of Production Engineering and Machine Tools, Leibniz Universität Hannover, Ottenbecker Damm 12, Stade, Germany*

ARTICLE INFO

ABSTRACT

In this paper, a 3D finite element modelling approach is presented to assess the effects of manufacturing defects within composite structures. The mesoscale modelling approach derives the stress-strain response of a composite structure from a representative structural element. A set of tensile and bending loads is used to compute its ABD-Matrix. The boundary conditions of the model are described in detail as is the extraction of the strain and curvature response. The derived stiffness from the presented modelling approach is compared to the classical lamination theory and the models' shortcomings are discussed. Finally, the influence of a gap, an overlap and two different-sized fuzzballs on the macroscopic mechanical properties of a composite structure are evaluated using the presented multiscale modelling approach, thereby providing stiffness matrices influenced by the defects for the use in global models of composite parts.

1. Introduction

Automated fibre placement (AFP) is an established production process to manufacture complex carbon fibre-reinforced polymer (CFRP) composite parts on an industrial scale. The complex nature of the AFP process though allows for the occurrence of process-induced defects, such as gaps, overlaps, tow-twists or fuzzballs [1]. Ideally, process-induced defects need to be addressed during layup, as a retroactive correction after curing is costly and, in cases with high requirements for structural integrity such as in the aviation industry, oftentimes not possible. This can result in production downtimes of up to 50% [2].

Therefore, research in online monitoring of the AFP layup process is being conducted [3–5]. Promising monitoring methods include laser scanning of the layup surface [4] and thermographic monitoring of the tows during layup [6–9]. Yet there still is a lack of understanding on how the defects influence the mechanical properties of a CFRP structure.

Research in assessing the effects of AFP process-induced defects mainly focuses on the effects of positioning defects such as gaps and overlaps, as these types of defects are oftentimes inevitable, such as in the layup of double curved surface-parts or when laying variable stiffness laminates [10–13]. It is generally found that single defects have

negligible impact on the elastic behaviour of a composite structure, whereas a reduction in tolerable strength might occur in dependency of structure size, defect size and defect positioning within the laminate. The accumulation of defects show a higher influence on the stiffness properties of composites [14].

The influence of twisted tows, gaps and overlaps on coupon and open-hole specimens under tension and compression loading were experimentally investigated by Croft et al. [15]. Seon et al. [16] investigate the influence of resin-filled voids on the strength and formulates a fatigue prognosis. While the investigated voids also result in comparable deflections within the fibre layers, foreign objects such as fuzzballs (Fig. 1) are not as easily characterised due to their irregular shape, fibre direction and fibre volume fraction. Thus, to this day, fuzzballs are only described regarding their formation and general effects [1]. This proves especially problematic when cured composite parts with internal fuzzballs need to be assessed for their structural integrity, as the mechanical effects of fuzzballs are not well described.

Numerical assessments investigating the impact of AFP process-induced defects have been conducted following different modelling strategies. As the in-plane and out-of-plane fibre waviness of the layers surrounding the defect has the most significant impact on the elastic response of a composite structure, the fibre waviness is often used as a

Fig. 1. Carbon fibre fuzzball on an uncured CFRP laminate during layup.

Fig. 2. Representative structural element (RSE) model frame and parameter definition.

modelling parameter for evaluating the effects of defects [10,14,17]. Another approach is to apply multiscale modelling techniques, thus assessing a defect in a mesoscale simulation within macroscale part analysis [18].

This paper presents a novel 3D finite element representative structural element (RSE) approach to numerically assess the impact of manufacturing-induced defects on the characteristic stiffness parameters of a thin-walled composite structure. Spanning several layers, the proposed detailed RSE especially allows for the detailed investigation of fuzzballs, which is currently missing in similar numerical modelling setups. The presented numerical approach deduces the stiffness parameters of a laminate region influenced by a defect and derives its adjusted ABD matrix in order to make the results usable in a multiscale simulation scheme. The presented simulation approach allows for high flexibility in modelling geometrically complex defects by being able to incorporate high-resolution geometric data from real-world measurements such as computer tomography or online detection techniques. As the setup of the boundary conditions follows the same presumptions of standard plate theories used for describing the elastic response of composite laminates, the model is suitable to be deployed in a multiscale simulation setup.

2. Representative structural element formulation

The representative structural element (RSE) presented in this paper is based on the unit-cell model developed by Hannig [19–21], which was developed to characterise the elastic bending behaviour of a morphing skin structure. In-house preliminary studies found that by extending the unit-cell model, it can describe the mechanical influence of production defects on thin-walled CFRP structures. The 3-dimensional cuboid RSE model represents a cut-out of a cured, planar CFRP structure with a shell-like deformable response. The size of the RSE model depends on the size of the heterogeneities to be investigated. The production defects typically are too large to accurately model the elastic structural response on a microstructural, i.e. lamina scale, yet they are too small to reasonably be modelled on a macroscopical structural scale. Hence the model is characterised by its mesoscale, utilising averaged material properties on the lamina level and outputting characteristic shell stiffness parameters for macroscopic structure simulations. The simulation scale is thus defined by the characteristic lengths of the manufacturing defect.

While Hannig mainly studied the influence of evenly distributed cracks which allow for periodic boundary conditions, the approach described in this paper concentrates on modelling singular, non-periodic and partly non-symmetric manufacturing defects within the laminate. The term "unit-cell", as was used by Hannig for his model, is thus misleading in the intended use case for this study and therefore replaced by the term "Representative Structural Element" (RSE).

The RSE is framed by eight corner nodes ① – ⑧, with an overall length L_x and an overall width L_y as shown in Fig. 2. The laminate thickness t as expected for a defect-free laminate defines the height of
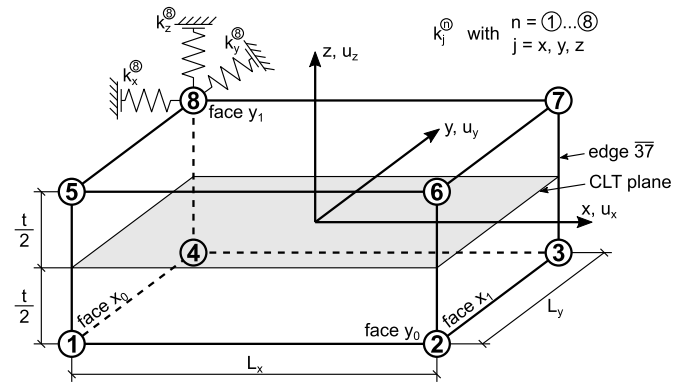
the frame. The framing corner nodes are independent of the model mesh. By defining constraints as described in Section 2.1, translational fixation of the corner nodes to the geometry of the RSE is ensured. Note that protrusion of the frame in the z-direction by the modelled geometry is allowed, while protrusion of the cutting faces x_0, x_1, y_0 and y_1 is not.

The corner nodes also act as load introduction points for the model. To reach numerical stability, the forces acting on the corner nodes ① – ⑧ must be equal and opposite, so that the total forces and moments acting on the RSE sum up to zero. Otherwise, the solution is ambivalent, as the model is not clamped in space by any boundary condition. Although global force and moment balance in theory should provide numerical stability, the model is further supported by weak ground springs in all translational directions at each corner node to counteract numerical instability. The spring stiffness k_j^n of each spring is arbitrarily set to $10^{-5} N/mm$ to ensure negligible influence on the elastic-mechanical response of the RSE.

The structural response of the RSE is comparable to that of a conventional, anisotropic shell element and can be used as such in macroscopic structure simulations. The material characteristics of such a composite shell element are typically calculated via classical lamination theory [22,23]. To be able to compare the structural response of the RSE to the classical lamination theory, the reference surface of the RSE model is positioned at a height of $t/2$ relative to the frame. The defect position in the thickness direction thus also influences the structural response of the RSE and is reflected in the stress-strain relation of the substituting shell element.

2.1. Boundary conditions

In contradiction to the approach described by Hannig in [20], the RSE presented in this paper does not solely include periodic boundary conditions. This stems mainly from the necessity for the RSE to run simulations of non-recurring production defects such as fuzzballs or tow-twists. In such cases, periodic boundary conditions might infer artificial stresses at the cutting faces of the RSE. This edge effect can be mitigated by increasing the RSE model size. However, this is not favourable from a researcher's point of view, as in doing so, the measurable effects of defects on the RSE structure decrease as well. Therefore, non-periodic boundary conditions potentially give a better understanding of the mechanical influence of defects on composite structures.

Nonetheless, periodicity can be assumed in some cases, for example when recurring defects such as gaps and overlaps are unavoidable due to limitations of the layup process. Also, by comparing the output of the RSE with non-periodic boundary conditions to the same RSE with periodic boundary conditions, the assumptions behind the given boundary conditions can be verified. For this reason, the presented RSE model defines two boundary condition sets: one with assumed periodicity and

one without.

Every node i of the model fulfils Eq. (1), in which the deformed co-ordinates $x = (x_x, x_y, x_z)^T$ are put in relation to the initial coordinates $X = (X_x, X_y, X_z)^T$ and the displacements $u = (u_x, u_y, u_z)^T$ of a node i [20].

$$x_i = X_i + u_i \tag{1}$$

Normalised reference coordinates $(\vartheta, \eta, \xi)^T$ relative to the governing frame can be defined for each node i according to Eq. (2). Note that ξ might protrude the interval [0, 1] within the region of a defect.

$$
\begin{aligned}
\vartheta_i &= \frac{X_{x,i} - X_{x,(1)}}{L_x} \\
\eta_i &= \frac{X_{y,i} - X_{y,(1)}}{L_y} \qquad \vartheta, \eta \in [0, 1] \\
\xi_i &= \frac{X_{z,i} - X_{z,(1)}}{t}
\end{aligned}
\tag{2}
$$

2.1.1. Periodic boundary conditions

When assuming periodicity, every node i on the face x_0, excluding the nodes on the vertical edges, is constrained in its movement to its respective opposing node on face x_1 and to all corner nodes ① - ⑧ in every translational movement according to Eq. (3).

$$
\begin{aligned}
u_i^{x_1} = u_i^{x_0} &+ (1 - \xi_i) \cdot (1 - \eta_i) \cdot (u_{(2)} - u_{(1)}) + (1 - \xi_i) \cdot \eta_i \cdot (u_{(3)} - u_{(4)}) \\
&+ \xi_i \cdot (1 - \eta_i) \cdot (u_{(6)} - u_{(5)}) + \xi_i \cdot \eta_i \cdot (u_{(7)} - u_{(8)})
\end{aligned}
\tag{3}
$$

Likewise, every pair of opposing nodes on faces y_0 and y_1 are constrained in every translational movement according to Eq. (4), again excluding the nodes on the vertical edges.

$$
\begin{aligned}
u_i^{y_1} = u_i^{y_0} &+ (1 - \xi_i) \cdot (1 - \vartheta_i) \cdot (u_{(4)} - u_{(1)}) + (1 - \xi_i) \cdot \vartheta_i \cdot (u_{(3)} - u_{(2)}) \\
&+ \xi_i \cdot (1 - \vartheta_i) \cdot (u_{(8)} - u_{(5)}) + \xi_i \cdot \vartheta_i \cdot (u_{(7)} - u_{(6)})
\end{aligned}
\tag{4}
$$

The nodes on the vertical edges $\overline{15}$, $\overline{26}$, $\overline{37}$ and $\overline{48}$ are constrained to their diagonally opposing edge node and to the corner nodes spanning the edges in every translational movement as shown in Eq. (5) and (6).

$$u_i^{\overline{37}} = u_i^{\overline{15}} + (1 - \xi_i) \cdot (u_{(3)} - u_{(1)}) + \xi_i \cdot (u_{(7)} - u_{(5)}) \tag{5}$$

$$u_i^{\overline{26}} = u_i^{\overline{48}} + (1 - \xi_i) \cdot (u_{(2)} - u_{(4)}) + \xi_i \cdot (u_{(6)} - u_{(8)}) \tag{6}$$

2.1.2. Non-periodic boundary conditions

When no periodicity is assumed, the nodes on each cutting face excluding the vertical edge nodes are constrained to the four corner nodes framing the respective face in x- and y-movement. Note that the displacement dependency of opposing nodes no longer is present. Movement in the z-direction is not constrained, as this would prohibit out-of-plane bending response of the model at the cutting faces. The exemplary constraints for each node on face x_0 is given in Eq. (7). All other faces are constrained accordingly to their framing corner nodes.

$$u_i^{x_0} = +(1 - \xi_i) \cdot (1 - \eta_i) \cdot u_{(1)} + (1 - \xi_i) \cdot \eta_i \cdot u_{(4)} + \xi_i \cdot (1 - \eta_i) \cdot u_{(5)} + \xi_i \cdot \eta_i \cdot u_{(8)} \tag{7}$$

The nodes on the vertical edges are constrained in x- and y-movement to the corner nodes spanning the edges, as is exemplarily shown for edge $\overline{15}$ in Eq. (8). Constraints for z-movement may be given at this point without hindering bending modes, but this might lead to local stress peaks in the thickness direction at the edges due to non-linear transverse strain and is therefore not implemented.

$$u_i^{\overline{15}} = +(1 - \xi_i) \cdot u_{(1)} + \xi_i \cdot u_{(5)} \tag{8}$$

2.2. Load cases

Six unique load cases are predetermined, corresponding to the six stress states of the stress-strain relation, as shown in Fig. 3 [20]. The macroscopic forces F are imposed on the framing corner nodes of the RSE, thus equally distributing the forces alongside the faces through the boundary conditions. The magnitude of the forces acting on the corner nodes is computed from the shear and moment fluxes n and m according to Table 1. The subscript index in conjunction with Fig. 3 denotes the

Table 1
Forces applied in the predetermined load cases.

case	load
1	$F_x = \frac{1}{4} \cdot n_x \cdot L_y$
2	$F_y = \frac{1}{4} \cdot n_y \cdot L_x$
3	$F_x = \frac{1}{4} \cdot n_{xy} \cdot L_x$ and $F_y = \frac{1}{4} \cdot n_{xy} \cdot L_y$
4	$F_x^b = \frac{1}{2} \cdot m_x \cdot \frac{L_y}{t}$
5	$F_y^b = \frac{1}{2} \cdot m_y \cdot \frac{L_x}{t}$
6	$F_x^b = \frac{1}{2} \cdot m_{xy} \cdot \frac{L_x}{t}$ and $F_y^b = \frac{1}{2} \cdot m_{xy} \cdot \frac{L_y}{t}$
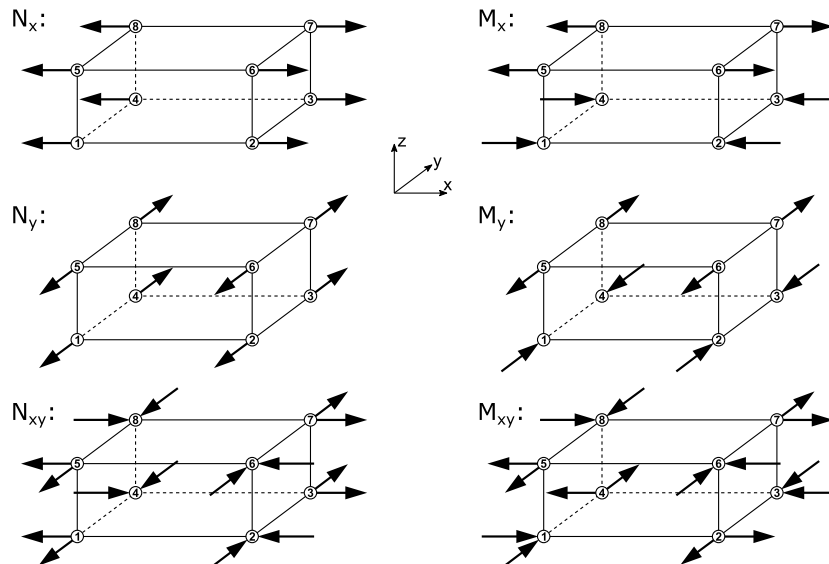
Fig. 3. Load cases applied to the RSE.

direction the force is acting upon each corner node.

2.3. Acquisition of structural response

To derive the stress-strain relation, the global strain and curvature response of the RSE has to be determined. The strain and curvature response of the RSE model can be extracted using solely the displacement of the corner nodes ① – ⑧, as described by Hannig [19].

The in-plane strain response of the RSE can be calculated directly by exploiting the macroscopic kinematic relations $\varepsilon_x = \partial u_x/\partial x$ and $\varepsilon_y = \partial u_y/\partial y$ for the strain in x- and y-direction and $\gamma_{xy} = \partial u_x/\partial y + \partial u_y/\partial x$ for the strain in x- and y-direction and $\gamma_{xy} = \partial u_x/\partial y + \partial u_y/\partial x$ for the shear strain. Thus, the strain response of the RSE directly derives from the averaged corner displacement, as is shown in Eq. (9) to (11). Note that a bending response of the RSE does not influence the calculation of the in-plane strain.

$$\epsilon_x = \frac{1}{4} \cdot \left(\frac{u_x^{(2)} - u_x^{(1)}}{L_x} + \frac{u_x^{(3)} - u_x^{(4)}}{L_x} + \frac{u_x^{(6)} - u_x^{(5)}}{L_x} + \frac{u_x^{(7)} - u_x^{(8)}}{L_x} \right) \tag{9}$$

$$\epsilon_y = \frac{1}{4} \cdot \left(\frac{u_y^{(3)} - u_y^{(2)}}{L_y} + \frac{u_y^{(4)} - u_y^{(1)}}{L_y} + \frac{u_y^{(7)} - u_y^{(6)}}{L_y} + \frac{u_y^{(8)} - u_y^{(5)}}{L_y} \right) \tag{10}$$

$$\gamma_{xy} = \frac{1}{4} \cdot \left(\frac{u_x^{(3)} - u_x^{(2)}}{L_y} + \frac{u_x^{(4)} - u_x^{(1)}}{L_y} + \frac{u_x^{(7)} - u_x^{(6)}}{L_y} + \frac{u_x^{(8)} - u_x^{(5)}}{L_y} \right)$$
$$+ \frac{1}{4} \cdot \left(\frac{u_y^{(2)} - u_y^{(1)}}{L_x} + \frac{u_y^{(3)} - u_y^{(4)}}{L_x} + \frac{u_y^{(6)} - u_y^{(5)}}{L_x} + \frac{u_y^{(7)} - u_y^{(8)}}{L_x} \right) \tag{11}$$

Due to the exploitation of the macroscopic kinematic relations, the derivation of the in-plane strain response is only applicable to small strains and displacements within the simulations, as will be discussed in Section 3.1.

The curvature response of the RSE is estimated via the angles of the vertical edges. Given a macroscopic shell structure, the infinitesimal curvatures κ_x and κ_y at each point in the structure can be described by Eq. (12) and (13).

$$\kappa_x = \frac{\partial^2 u_z}{\partial x^2} = \frac{\partial \varphi_x}{\partial x} \tag{12}$$

$$\kappa_y = \frac{\partial^2 u_z}{\partial y^2} = \frac{\partial \varphi_y}{\partial y} \tag{13}$$

The angular change of the vertical edges respective to the x- or y-axis can be derived by exploiting the scalar product of the directional vectors of the vertical edges and the base vectors $e_x = (1, 0, 0)^T$ and $e_y = (0, 1, 0)^T$. The angular change $\Delta \varphi_x$ and $\Delta \varphi_y$ for the edge $\overline{15}$ is exemplarily given in Eq. (14). The angular changes of the other three vertical edges are calculated accordingly.

$$\Delta \varphi_x^{\overline{15}} = \frac{\pi}{2} - acos\left(\frac{e_x \cdot \left(x_{(5)} - x_{(1)} \right)}{x_{(5)} - x_{(1)}} \right)$$
$$\Delta \varphi_y^{\overline{15}} = \frac{\pi}{2} - acos\left(\frac{e_y \cdot \left(x_{(5)} - x_{(1)} \right)}{x_{(5)} - x_{(1)}} \right) \tag{14}$$

By inserting Eq. (14) in the macroscopic curvature definitions from Eq. (12) and (13), and by further calculating the mean of the two opposite vertical edge pairs, the curvature of the RSE can be obtained solely by the displacement of the corner nodes in Eq. (15) and (16).

$$\kappa_x = \frac{1}{2} \cdot \left(\frac{\Delta \varphi_x^{\overline{26}} - \Delta \varphi_x^{\overline{15}}}{L_x} + \frac{\Delta \varphi_x^{\overline{37}} - \Delta \varphi_x^{\overline{48}}}{L_x} \right) \tag{15}$$

$$\kappa_y = \frac{1}{2} \cdot \left(\frac{\Delta \varphi_y^{\overline{37}} - \Delta \varphi_y^{\overline{26}}}{L_y} + \frac{\Delta \varphi_y^{\overline{48}} - \Delta \varphi_y^{\overline{15}}}{L_y} \right) \tag{16}$$

Following the same underlying principle, the macroscopic twisting

curvature of the RSE can be expressed as shown in Eq. (17).

$$\kappa_{xy} = \frac{\partial^2 u_z}{\partial x \partial y} = \frac{\partial \varphi_{xy}}{\partial (\Delta x, \ \Delta y, \ 0)^T} - \frac{\partial \varphi_{xy}}{\partial (\Delta x, \ -\Delta y, \ 0)^T} \tag{17}$$

The angular change $\Delta \varphi$ of the vertical edges now must reflect the diagonal twisting κ_{xy} of the vertical edges and thus be calculated in relation to a diagonal base vector as defined in Eq. (18). Special care must be taken with sign conventions to keep positive curvature definitions consistent.

The infinitesimal reference lengths L_{xy} for calculating the twisting curvature κ_{xy} in Eq. (17) can be easily calculated to $L_{xy} = 0,5 \cdot (\sqrt{2}L_x + \sqrt{2}L_y)$. This however introduces one important constraint to the RSE model, as the resulting formula for calculating the twisting curvature of the RSE shown in Eq. (19) only holds for quadratic RSE models (i.e. $L_x = L_y$).

$$\Delta \varphi_{xy}^{\overline{15}} = \frac{\pi}{2} - acos\left(\frac{(e_x + e_y) \cdot \left(x_{(5)} - x_{(1)} \right)}{\sqrt{2} \cdot \| x_{(5)} - x_{(1)} \|} \right) \Delta \varphi_{xy}^{\overline{26}}$$
$$= \frac{\pi}{2} - acos\left(\frac{(e_x - e_y) \cdot \left(x_{(6)} - x_{(2)} \right)}{\sqrt{2} \cdot \| x_{(6)} - x_{(2)} \|} \right) \Delta \varphi_{xy}^{\overline{37}}$$
$$= \frac{\pi}{2} - acos\left(\frac{(e_x + e_y) \cdot \left(x_{(7)} - x_{(3)} \right)}{\sqrt{2} \cdot \| x_{(7)} - x_{(3)} \|} \right) \Delta \varphi_{xy}^{\overline{48}}$$
$$= \frac{\pi}{2} - acos\left(\frac{(e_x - e_y) \cdot \left(x_{(8)} - x_{(4)} \right)}{\sqrt{2} \cdot \| x_{(8)} - x_{(4)} \|} \right) \tag{18}$$

$$\kappa_{xy} = \frac{\Delta \varphi_{xy}^{\overline{37}} - \Delta \varphi_{xy}^{\overline{15}}}{\frac{1}{2} \left(\sqrt{2}L_x + \sqrt{2}L_y \right)} - \frac{\Delta \varphi_{xy}^{\overline{26}} - \Delta \varphi_{xy}^{\overline{48}}}{\frac{1}{2} \left(\sqrt{2}L_x + \sqrt{2}L_y \right)} \tag{19}$$

A more thorough explanation of the above equations can be found in [19].

2.4. Stiffness representation

A standard representation of the mechanical properties of a composite structure is given by the classical lamination theory, within which the macroscopic constitutive relation is given in Eq. (20). The underlying assumptions for the classical lamination theory are similar to the Kirchhoff-Love plate theory. Herein, a thin-walled plate structure is represented by its mid-surface, allowing for both in-plane deformation and out-of-plane bending [22–25].

$$\begin{bmatrix} n \\ m \end{bmatrix} = \begin{bmatrix} A & B \\ B & D \end{bmatrix} \cdot \begin{bmatrix} \epsilon \\ \kappa \end{bmatrix} \tag{20}$$

The force and moment fluxes acting on the mid-surface are denoted in $n = (n_x, n_y, n_{xy})^T$ and $m = (m_x, m_y, m_{xy})^T$, whereas $\varepsilon = (\varepsilon_x, \varepsilon_y, \gamma_{xy})^T$ and $\kappa = (\kappa_x, \kappa_y, \kappa_{xy})^T$ denote the strains and curvatures acting on the reference plane. The stiffness matrix is a 6 × 6 matrix which links the force and moment fluxes to the strains and curvatures of thin-walled composites similar to Hooke's law and is generally referred to as ABD matrix due to its submatrices *A, B* and *D* [22,23]. Herein, A_{ij} denotes the in-plane behaviour, D_{ij} denotes the out-of-plane behaviour and B_{ij} denotes the coupling characteristics of a composite shell.

The six load cases defined in Section 2.2 are set such that for each load case only one term in *n* and *m* is non-zero. When inverting the constitutive relation in Eq. (20) as shown in Eq. (21), each row of the inverted ABD matrix can then be solved uniquely by the corresponding structural response of the RSE.

$$
\begin{bmatrix}
\epsilon_x \\
\epsilon_y \\
\epsilon_{xy} \\
-- \\
\kappa_x \\
\kappa_y \\
\kappa_{xy}
\end{bmatrix}
=
\left[
\begin{array}{ccc|ccc}
A_{11}{'} & A_{12}{'} & A_{16}{'} & B_{11}{'} & B_{12}{'} & B_{16}{'} \\
A_{21}{'} & A_{22}{'} & A_{26}{'} & B_{21}{'} & B_{22}{'} & B_{26}{'} \\
A_{61}{'} & A_{62}{'} & A_{66}{'} & B_{61}{'} & B_{62}{'} & B_{66}{'} \\
\hline
B_{11}{'} & B_{12}{'} & B_{16}{'} & D_{11}{'} & D_{12}{'} & D_{16}{'} \\
B_{21}{'} & B_{22}{'} & B_{26}{'} & D_{21}{'} & D_{22}{'} & D_{26}{'} \\
B_{61}{'} & B_{62}{'} & B_{66}{'} & D_{61}{'} & D_{62}{'} & D_{66}{'}
\end{array}
\right]
\cdot
\begin{bmatrix}
n_x \\
n_y \\
n_{xy} \\
-- \\
m_x \\
m_y \\
m_{xy}
\end{bmatrix}
\quad (21)
$$

By inverting the inverse ABD matrix, the representative stiffness properties of the RSE model are finally obtained. It should be noted that the ABD matrix derived from the RSE model allows for non-symmetry of its constituents, as every ABD term is calculated independently. Thus, the non-symmetric mechanical response of the RSE is also reflected in the derived ABD matrix.

3. Application and discussion

3.1. RSE model validation

The consistency of the RSE model was validated against the classical laminate theory in a numerical comparison. The laminate layup was arbitrarily chosen to be [0°, 30°, 60°, 45°] for all simulations with a ply thickness $t_{ply} = 175\mu m$, resulting in a total laminate thickness $t = 0.7mm$. The non-symmetric laminate configuration allows for a fully occupied ABD matrix with all non-zero terms. The reference ABD matrix derived via classical lamination theory is shown in Eq. (22). Note that all entries are far greater than zero, allowing for a relative comparison of the ABD derived by the RSE model to the classical lamination theory.

$$
ABD^{CLT} =
\begin{bmatrix}
58994.7 & 18184.0 & 18764.6 & -6490.8 & 1683.0 & 1317.1 \\
 & 31521.4 & 18764.6 & 1683.0 & 3124.8 & 2288.8 \\
 & & 19948.4 & 1317.1 & 2288.8 & 1683.0 \\
 & & & 2927.8 & 644.3 & 612.2 \\
 & sym. & & & 964.6 & 612.2 \\
 & & & & & 716.4
\end{bmatrix} MPa
$$
$$(22)$$

The quadratic, reduced 3D continuum elements (C3D20R) were assigned "engineering constants" material properties within Abaqus 2020. The mechanical properties of the unidirectional lamina used in the validation study were taken from the World Wide Failure Exercise III and are listed in Table 2 [26].

The structural response ABD^{RSE} derived from the RSE is compared to the classical lamination theory ABD^{CLT} shown in Eq. (22). The relative difference ΔABD is calculated according to Eq. (23), which allows for a comparison of the RSE to the classical lamination theory on a percentage basis. Positive entries hereby indicate a stiffer response of the RSE compared to the classical lamination theory.

$$
\Delta ABD_{ij} = \frac{\left(ABD_{ij}^{RSE} - ABD_{ij}^{CLT} \right)}{ABD_{ij}^{CLT}}
\quad (23)
$$

The validation model size is set to $L_x = L_y = 5mm$. As was mentioned in Section 2.3, the twisting response of the RSE only holds for quadratic

Table 2
Mechanical properties for the unidirectional lamina IM7 as prescribed in WWFE III.

E_1	165	GPa	ν_{21}	0.34	G_{12}	5.6	GPa
E_2	9	GPa	ν_{31}	0.34	G_{13}	5.6	GPa
E_3	9	GPa	ν_{32}	0.5	G_{23}	2.8	GPa

RSE models. The mesh size is set to hold two elements per ply in the thickness direction, with the in-plane to out-of-plane aspect ratio set to 2.

The load collective of the validation study was chosen for each load case such as that normal strains do not exceed 0.25% and shear strains do not exceed 0.5% within the RSE model elements, thereby complying with the presumption of small deformations.

Fig. 4 (left) shows the relative deviations between the ABD^{RSE} matrix terms of the validation model and the ABD^{CLT} from the classical lamination theory. With a mean deviation of 0.122%, the extensional stiffness matrix A shows good consistency to the classical lamination theory, as does the D matrix with a mean deviation of -0.085%.

The greatest deviations can be found in the coupling matrices B with deviations of up to -1.903%. More notably it was found that the upper right B matrix of the ABD^{RSE} matrix is not symmetrical to the bottom left B matrix. This shows a clear discrepancy to the classical lamination theory, where such behaviour is not possible due to the underlying assumption of linear elasticity. From the author's perspective, the non-symmetry of the B matrices is to be explained by the difficulty of accurately modelling the bending behaviour of quadrilateral elements within finite element simulations [27]. This becomes apparent when examining the deviation of the inverse ABD matrices from both RSE and classical lamination theory ΔABD^{-1} (Fig. 4, right). It can be clearly seen that the strain and curvatures in the bending load cases M_x, M_y and M_{xy} deviate from the expected values from the classical lamination theory, whereas the load cases with tensile forces N_x, N_y and N_{xy} show almost no deviation. The material properties used in this study further amplify this error due to their high anisotropy (Table 2). The latter also explains the overall higher deviations of the RSE to the classical lamination theory compared to the findings in [19,20].

The validation study found no significant difference when comparing the simulation outcome of the two boundary condition sets. The greatest deviation between any of the ΔABD terms of the RSE response with periodic boundary conditions compared to the RSE response with non-periodic boundary conditions was measured to be smaller than $3.26e^{-5}\%$, thus proving the applicability of the non-periodic boundary condition set for defect-free laminates. It should be noted, however, that a notably higher deviation between the two boundary condition sets is to be expected for RSE models containing a non-symmetric defect.

Finer meshing showed no significant influence on the RSE outcome. However, this might only hold for simulations of defect-free laminates. When analysing production defects, non-linear force progressions are to be expected within the laminate, which should be addressed by sufficiently decreasing mesh sizes in affected areas.

3.2. Numerical assessment of defects

In the following sections, the structural influence of three different AFP-specific production-induced defects is examined with the RSE model described above. Namely, simplified models of gaps, overlaps and fuzzballs are analysed for a cured composite structure. An overview of various AFP-specific production-induced defects is given in [1].

Different modelling approaches were used for the definition of the geometry and material characteristics of the examined defects. These are explained in detail in their respective sections. The layers above and below the defects are simplified to not vary in their thickness. As the aim is to simulate curing cycles with soft tooling, i.e. with a vacuum bagging during autoclave curing, this is a valid assumption [10]. This must also be taken into account when comparing the resulting mechanical properties to findings where hard tooling was used during the autoclave cycle, as defects with out-of-plane geometric deviations then affect all neighbouring layers both in their local geometry and their inherent local fibre volume fraction distribution [12,28].

Layers placed on top of defects are influenced by the defect through imposed out-of-plane fibre waviness [29]. This is reflected in the RSE model by adjusting the local material coordinate system of each

ΔABD in %

0.198	0.435	0.407	0.003	0.592	0.61
0.004	0.024	0.006	0.037	0.026	0.026
-0.004	0.026	-0.0	0.035	0.022	0.021
0.599	-1.384	-1.903	0.012	-0.463	-0.394
-0.157	0.014	-0.069	0.028	0.0	-0.005
-0.125	0.029	-0.05	0.034	0.011	0.01

ΔABD^{-1} in %

0.0	-0.0	-0.0	-0.0	0.0	-0.0
0.0	0.0	0.0	-0.0	0.0	0.0
0.0	-0.0	0.0	-0.0	-0.0	-0.0
0.107	0.125	-0.181	0.022	-0.003	-0.029
0.143	0.124	-0.186	0.023	-0.007	-0.02
0.096	0.122	-0.189	0.021	-0.008	-0.017

Fig. 4. Deviation of the validation RSE compared to the classical lamination theory, shown for the ABD matrix (left) and the inverse ABD matrix (right) in%.

element, such as that the material coordinate system is aligned to the fibre direction vector as derived for the geometrical centre of each element. With a sufficiently fine mesh in areas affected by the defect, the out-of-plane fibre waviness is thus physically reflected in the RSE model.

All simulations containing defects are based on the following underlying sizing of the RSE. The RSE size is fixed to 40 mm x 40 mm with an orthotropic, alternating layup consisting of 9 layers starting in the x-direction with a ply thickness of $t = 175\mu m$. Defects are placed in layer 5. Fuzzballs are placed on top of layer 5. The material parameters used are the same as before, given in Table 2. Non-periodic boundary conditions were applied, and the load flux was consistently set to $1N/mm$ for each load case.

Meshing is done with a discretization of $100\mu m$ in planar directions and of $87.5\mu m$ in the thickness direction of the RSE. In-plane meshing is held constant only within the rectangular bounding box of the defect and an additional 10% beyond. Outside this refined defect area, the mesh size exponentially increases with a factor of 1.25 per element, thus allowing for a bigger RSE with reasonable solving time. The mesh in thickness direction adapts to deviating local thicknesses with a logarithmic mesh size distribution towards the ply centre while maintaining a thickness of $87.5\mu m$ for the biggest element where possible. The corresponding ABD matrix for a defect-free layup calculated via classical lamination theory is shown in Eq. (24). Mechanical response of defects is presented in relative terms to ABD^{CLT}, following the same procedure as in Eq. (23). The maximum deviation of the RSE response for the defect-free layup was no greater than 0.001%, attributing to the orthotropic layup, which does not yield any coupling characteristics.

w_{gap}, the gap thickness at its centre t_{gap}, the width $w_{gap,min}$ at which the gap thickness t_{gap} is held constant, and the width $w_{gap,resin}$ at which the gap is filled with pure resin. The gap geometry is presumed to be symmetric to the gap centre. Fig. 5 shows the defining parameters in the cross-sectional view of a laminate.

The thickness of the gaps in the transition areas is given in Eq. (25) as a function of the control variable s orthogonal to the gap centre vector. Note that a gap thickness of $t_{gap} = 0\mu m$ is allowed, resulting in a contact of the top and bottom plies adjacent to the gap.

$$t_{gap}(s) = \left(t_{ply} - t_{gap}\right) \cdot \left(3 \cdot \left(\frac{2 \cdot \left|s - w_{gap,\,min}/2\right|}{w_{gap} - w_{gap,\,min}}\right)^2 - 2 \cdot \left(\frac{2 \cdot \left|s - w_{gap,\,min}/2\right|}{w_{gap} - w_{gap,\,min}}\right)^3\right)$$
$$+ t_{gap}$$

(25)

The smooth transition avoids sharp direction changes of the fibre direction vectors of adjacent layers, thus better reflecting the out-of-plane fibre waviness in those layers. In contrast to [28], the layers surrounding the defect are not altered, as a soft tooling is considered in the assumed use case.

The defining parameters for gaps and overlaps can be directly obtained through micrographs of such defects. There exist analytical formulas in the literature for predicting the defining defect parameters, either as a function of the overall gap width w_{gap} [28] or as a function of the initial gap width $w_{gap,init}$ during layup [10]. Latter correlations are deemed especially useful, as they allow for an analysis of the influence of detected defects online during layup. Belnoue et al. [30] even presented
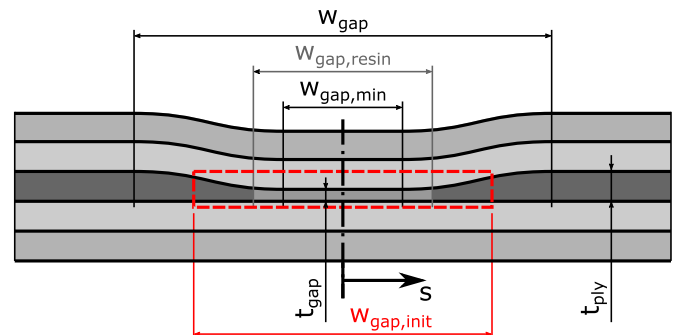
$$ABD^{CLT} = \begin{bmatrix} 151631.1 & 4850.1 & 0 & & & \\ 4850.1 & 124157.9 & 0 & & 0 & \\ 0 & 0 & 8820.0 & & & \\ & & & 36954.1 & 1002.6 & 0 \\ & 0 & & 1002.6 & 20056.6 & 0 \\ & & & 0 & 0 & 1823.3 \end{bmatrix} MPa$$

(24)

3.2.1. Gaps

The definition of the gap geometry is inspired by [28]. A gap is modelled by four distinct descriptive parameters: The overall gap width

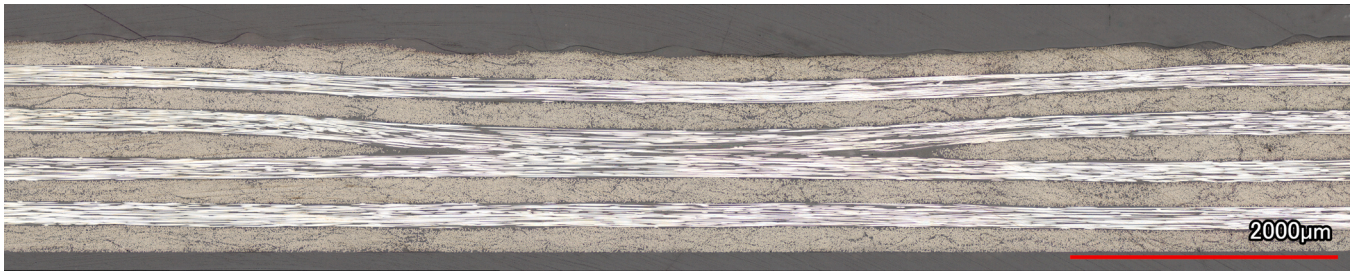**Fig. 5.** Geometric definition of gaps.

Fig. 6. Micrograph of a sample gap.

a sophisticated modelling technique for predicting the material flow during compaction, which holds the potential to not only predict the defect geometry, but also to predict the distribution of the local fibre volume fraction.

In the following, an example case of a gap is shown and discussed. The defining defect parameters are obtained from the analysis of a micrograph of a test specimen manufactured with an in-house automated fibre placement machine [31]. The defect was inserted in ply 5 by adjusting the layup code so that the corresponding tows were misplaced by half a tow-width at the defect position.

Fig. 6 shows the micrograph of the evaluated gap. The thickness values of the individual plies were extracted from the micrographs by manually tracing the ply borders with spline curves (Fig. 7). Note that the top surface of ply 9 is not as smooth as the borders beneath due to the soft tooling used in the autoclave. The mean ply thickness for all plies, excluding ply 5 featuring the gap, is calculated to be $t_{mean} = 175.1\mu m$ with a standard deviation of $t_{std} = 11.9\mu m$. In order to maintain comparability to the reference stiffness, as given in Eq. (24), the ply thickness in the simulation was consistently set to $t^i_{ply} = 175\ \mu m$.

The extracted gap width w_{gap} was defined as the length where ply 5 protrudes the standard deviation band $t_{mean} \pm t_{std}$, resulting in $w_{gap} = 6.01mm$. The centre gap width $w_{gap,min}$ was defined following $t_{ply5} < 10\mu m$, which results in $w_{gap,min} = 2.29\mu m$. The gap thickness is set to $t_{gap} = 0\mu m$. As described above, the gap is further simplified to be symmetric to its centre. Lastly, the resin-rich area is manually measured to a width of $w_{gap,resin} = 4.20\mu m$.

The stiffness degradation effect of the gap on the composite structure is shown in Fig. 8. The gap clearly shows a reduction in the in-plane stiffness of the RSE, with a pronounced stiffness reduction of 2.12% in the travel direction of the gap and a reduction of 1.40% transversal to the gap. The structural response transversal to an in-plane load is reduced by 2.30%, whereas the shear stiffness is also reduced by 1.28%.

The gap does introduce coupling of in-plane stress fluxes to the bending response of the structure. The magnitude of the coupling stiffness is deemed to be non-negligible with the highest entry in the B matrix reaching $-1805.1N$, thus influencing the buckling behaviour of composite structures with embedded gaps.

The highest relative degradations compared to the defect-free laminate response can be observed in the flexural rigidity of the RSE.
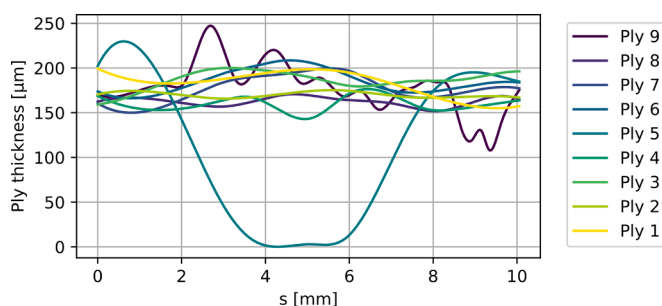
Transversal to the gap, the stiffness reduction exceeds 5.16%. This can be traced back to the reduction of the inertia tensors of the plies above the gap, as they follow the defect geometry and thus shift towards the referencing plane. Note that in this study, no experimental tests were conducted to validate the simulation results.

3.2.2. Overlaps

Overlaps are defined identically to gaps by replacing the indices *gap* with *overlap* in Eq. (25). The overlap geometry is defined through $t_{overlap} > t_{ply}$, resulting in a protruding geometry. Furthermore, no pure resin zones are defined for overlaps.

The micrograph of an example overlap is shown in Fig. 9 and the respective ply thicknesses are shown in Fig. 10. The mean ply thickness of the example overlap is measured to be $t_{mean} = 173.3\mu m$ with a standard deviation of $t_{std} = 12.2\mu m$. Again, the ply thickness in the RSE is set to $t^i_{ply} = 175\ \mu m$ for comparability.

Following the same strategy as for the gap, the overlap geometry is measured to $w_{overlap} = 7.96mm$. The maximum thickness is measured to be $t_{overlap} = 383.4\mu m$. Note that the observed overlap thickness $t_{overlap}$ is higher than the expected overlap thickness, which would be $2 \cdot t_{ply} = 346.6\mu m$. The centre width of the overlap is simplified to be $t_{overlap,min} = 0\mu m$, as the thickness course of ply 5 does not indicate a flat plateau in the centre of the overlap. As for the gap, the overlap in the RSE is simplified to be symmetric to its centre.

In contrast to the gap, the overlap shows an increase in stiffness for all loading cases except for one notable exception, namely for the loading transversal to the overlap (Fig. 11). The increase in stiffness longitudinal to the gap of 2.27% is expected, as the additional fibre material in the overlap stiffens the structure. Transversally, however, the material surplus mainly causes an out-of-plane fibre waviness of the layers above, thus weakening the overall structural response and leading to a stiffness reduction of 0.54%.

Again, as was the case for the gap, the overlap shows some coupling characteristics between in-plane stresses and bending response. The positive values should not be regarded as being comparably better to the response of the gap, as they only determine the direction of the bending response of the composite structure.

The highest increase in bending response can be observed in the D matrix, where the response for twisting is hindered up to 4.52% by the overlap. As for the in-plane stiffness, the bending rigidity is increased more in direction of the overlap as opposed to the transversal direction. Again, no experimental tests were conducted to validate the simulation results.

3.2.3. Fuzzballs

The presented RSE model especially excels at calculating the mechanical behaviour of composite structures with complex, three-dimensional geometrical defects. An example of such defects are fuzzballs (Fig. 1), which naturally occur in the AFP head through friction and abrasion of the tows with the routing parts of the AFP end-effector. This abrasion leads to an accumulation of fibres, resin or both, depending on the AFP machine. If the fuzzball is large enough, it may fall onto the composite layup and form a foreign object defect, if not manually
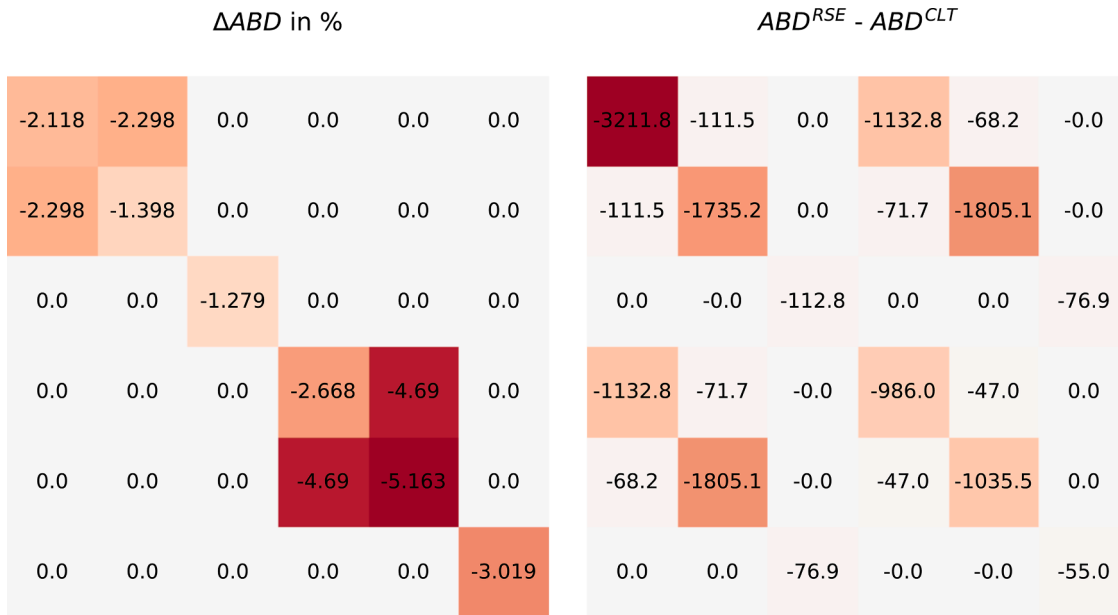

Fig. 7. Thickness of individual plies in the sample with a gap.

ΔABD in %

$ABD^{RSE} - ABD^{CLT}$

Fig. 8. Relative (left) and absolute (right) impact of the gap on the stiffness of the RSE.
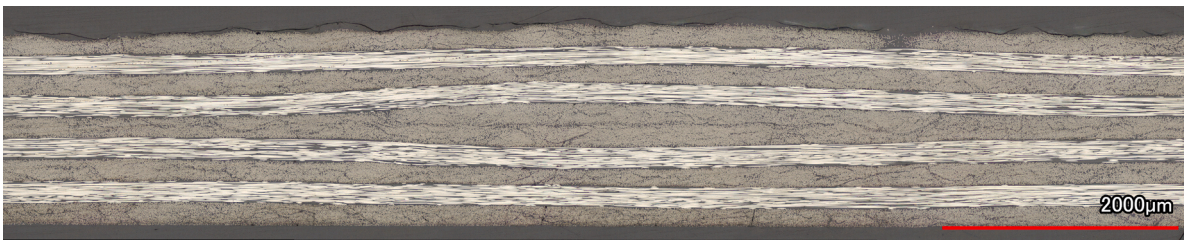

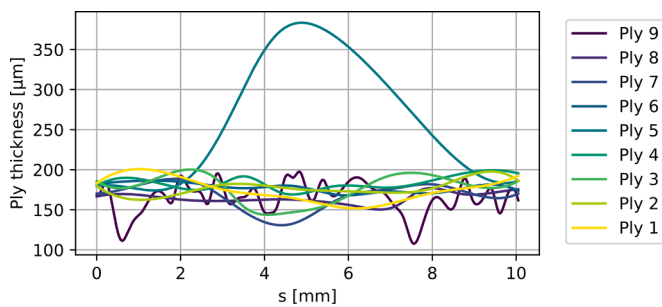**Fig. 9.** Micrograph of a sample overlap.

Fig. 10. Thickness of individual plies in the sample with an overlap.

removed before laying the next composite layer [1].

The geometric characterisation of fuzzballs is not as straightforward as for the other defects, as descriptive parameters are too general to accurately describe the defect. Therefore, to acquire the geometry of cured fuzzballs within a laminate, a flat CFRP laminate consisting of 9 plies was produced with an in-house automated fibre placement machine [31]. Fuzzballs in various sizes, provided by an industrial serial production, were intentionally placed on top of layer 5 of the test laminate. The test laminate was cured in an autoclave following the cure cycle recommended for the HexPly® 8552 AS4 material [32] used. Lastly, test specimens containing the fuzzballs were cut out of the cured laminate and examined by computer tomography (CT). The CT scans featured a resolution of 12μm/voxel.

The data obtained by CT were segmented in the software ORS

Dragonfly [33], labelling each voxel with either *background, laminate, fuzzball* or *pores*. Segmentation had to be done manually for the fuzzballs and the laminate, as the contrast between the fuzzball and the surrounding layers did not allow for reliable characterisation by automated means, i.e. deep learning methods. After segmenting the CT data, a volume thickness map for each fuzzball is created, specifying the height of the fuzzball at the corresponding in-plane position by counting the voxels labelled with either *fuzzball* or *pores* at that position and then multiplying it with the voxel resolution.

Air pockets within the fuzzball are also considered for implementation in the simulation model. To obtain a practicable volume thickness map of the porous region, a convex hull is generated around identified pores.

The RSE modelling of two selected fuzzballs, which differ in their size, shall be shown in this paper. The volume thickness maps and overall dimensions for the fuzzballs are given in Fig. 12 and Fig. 13.

The fuzzball is represented in the RSE by a separate layer in the layup. The z-values of the cornering nodes of each fuzzball element are taken from the volume thickness map described above. Extrapolation allows estimating the fuzzball thickness at positions in-between the finite values of the volume thickness map so that meshing can be done independently from a given volume thickness map. Note that non-hexahedral elements such as pyramids (C3D5) and prisms (C3D6) are used at the sloping borders of the fuzzball mesh where needed (Fig. 14).

Elements representing the cured fuzzball material are given estimated isotropic material characteristics with $E_{fuzz} = 9GPa$ and $\nu_{fuzz} = 0.35$, thus simplifying fuzzball material characteristics to pure resin material. It should be noted that although micrographs of cured fuzzballs are characterised by their resin surplus, they do also contain fibres

ΔABD in %

2.269	0.594	0.0	0.0	0.0	0.0
0.594	-0.54	0.0	0.0	0.0	0.0
0.0	0.0	1.221	0.0	0.0	0.0
0.0	0.0	0.0	4.357	2.994	0.0
0.0	0.0	0.0	2.994	3.617	0.0
0.0	0.0	0.0	0.0	0.0	4.524

ABD^{RSE} - ABD^{CLT}

3441.2	28.8	-0.0	1837.1	33.0	-0.0
28.8	-670.5	-0.0	32.5	817.2	-0.0
0.0	0.0	107.7	-0.0	-0.0	95.0
1837.1	32.5	-0.0	1610.2	30.0	-0.0
33.0	817.2	-0.0	30.0	725.4	-0.0
-0.0	-0.0	95.0	0.0	0.0	82.5

Fig. 11. Relative (left) and absolute (right) impact of the overlap on the stiffness of the RSE.
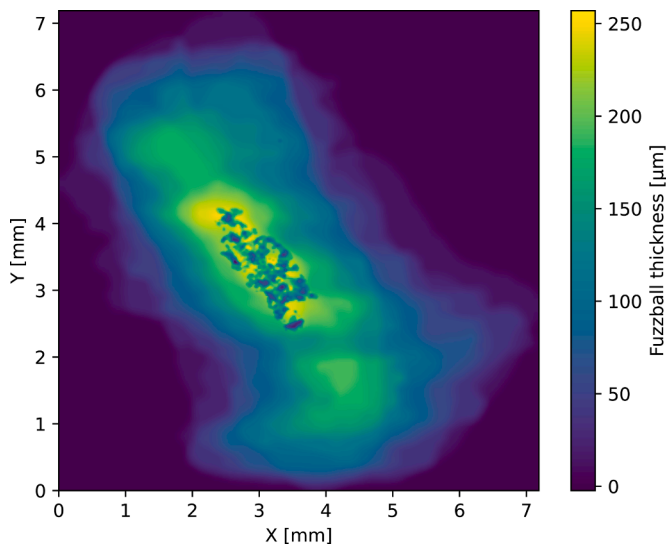

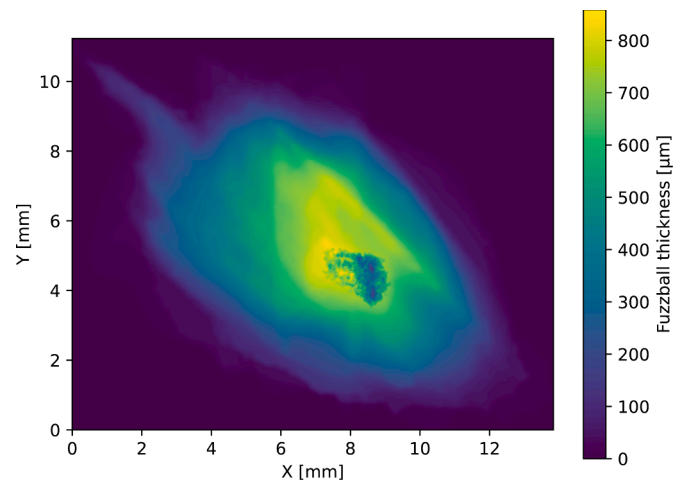**Fig. 12.** CT height profile of a small fuzzball with visible pores.

Fig. 13. CT height profile of a large fuzzball with visible pores.

without clear orientation. This should have an impact on the material behaviour of the fuzzball material. However, the mechanical characteristics of cured fuzzballs cannot be obtained through mechanical testing. As the effect of out-of-plane fibre waviness is expected to have a far greater impact on the overall mechanical response of the RSE, the simplified elastic behaviour of the fuzzball material is thus deemed sufficient.

Areas characterised by the occurrence of pores are nested within the fuzzball layer and are given isotropic material characteristics with $E_{pores} = 3GPa$ and $v_{pores} = 0.35$. Following the same presumption as before, the layers surrounding the fuzzballs are simplified to not vary in their thickness.

The simulation outcome of the small fuzzball is depicted in Fig. 15. When evaluating the diagonal entries of the extensional stiffness parameters in the *A* matrix, it can be shown that the small fuzzball has a very small impact on the most critical composite characteristics, i.e. the stiffness is reduced by less than 0.1% when in-plane loads are applied in either layer direction. The shear stiffness even shows an increase of

0.051%. The transverse stiffness shows a reduction of 0.58% relative to the defect-free layup.

The entries in the coupling matrices *B*, which are zero in the defect-free layup, are now all non-zero, meaning that an in-plane stress state will also induce an ever so slight bending response of the structure containing the defect (and vice versa). Interestingly, although the defect is non-symmetric, the ABD matrix maintains its symmetry along the diagonal.

The entries of the *D* matrix, defining the bending response of the structure to moment fluxes, show the highest deviations from the defect-free layup. The bending stiffness is increased alongside the diagonal, which can be explained by higher inertia tensors of the top plies, resulting from the out-of-plane displacement induced by the defect. This is a notable observation, as the fuzzball might therefore increase the buckling stability of the structure in case of compression loading, as was partially observed in [34]. However, the reduction in the transverse bending response might also counteract the postulated increase in buckling stability.

The larger fuzzball, which has a more significant impact on the out-of-plane fibre waviness of the top plies, shows a similar, yet stronger
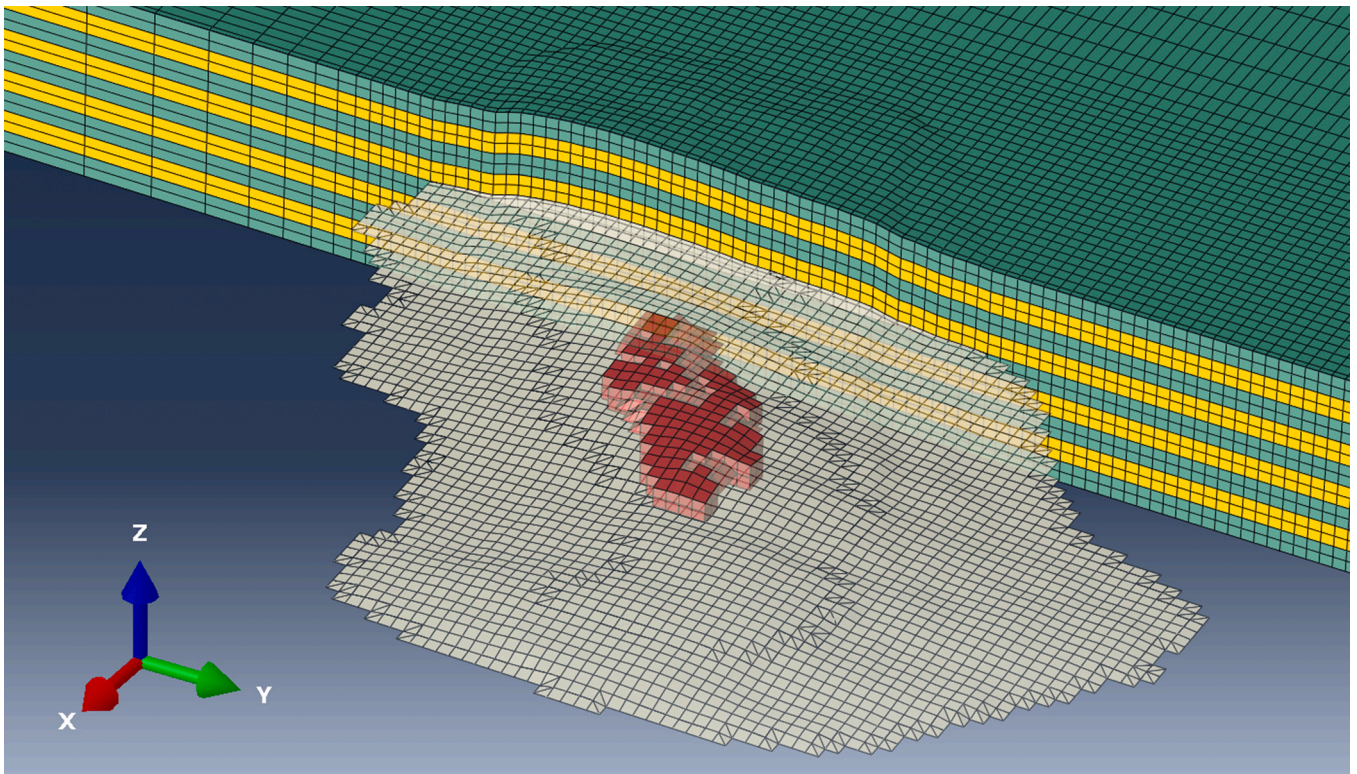
Fig. 14. Cut-out view of the RSE containing the small fuzzball (white) with its porous area (red).

ΔABD in %

$ABD^{RSE} - ABD^{CLT}$

Fig. 15. Relative (left) and absolute (right) influence of the small fuzzball on the stiffness of the RSE.

structural response of the RSE compared to the small fuzzball. The extensional stress responses of the RSE, which resemble the most relevant engineering parameters of a composite, now show a reduction of 0.543% in the x-direction and a reduction of 0.636% in the y-direction (Fig. 16). Once again, an increase in bending stiffness can be observed. It should be noted, however, that the overall bending stiffness of the laminate might be decreased, as the out-of-plane fibre waviness caused by the fuzzball negatively influences stress distribution along the fibres. Also, the fuzzball might act as a crack initiation point, thus increasing the risk of delaminations. Strength analyses for the defects are not

conducted in this paper, though the presented RSE approach provides the ability to incorporate sophisticated failure modelling approaches for laminates, such as implementing cohesive elements for delamination analysis [35] or the Puck failure criterion [36].

When comparing the mechanical influence of the small fuzzball to the large fuzzball, it should be noted that the RSE model size has not changed. The ratio of the characteristic defect size to the RSE model size has a non-negligible influence on the response of the RSE and must therefore be considered. This poses a difficulty when assessing geometrically complex defects such as fuzzballs, as a characteristic
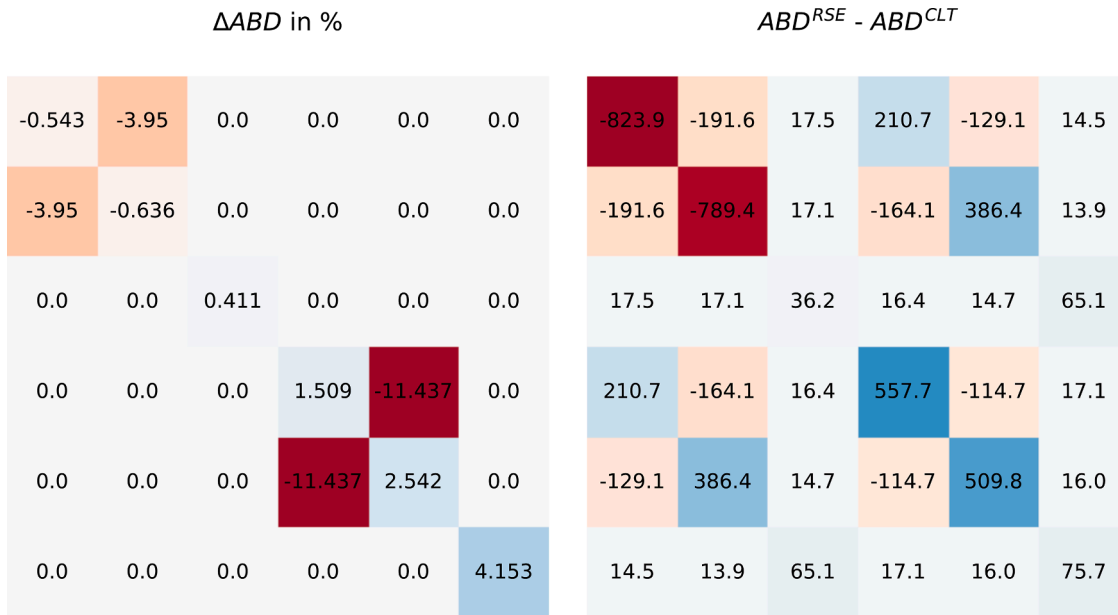
ΔABD in %

-0.543	-3.95	0.0	0.0	0.0	0.0
-3.95	-0.636	0.0	0.0	0.0	0.0
0.0	0.0	0.411	0.0	0.0	0.0
0.0	0.0	0.0	1.509	-11.437	0.0
0.0	0.0	0.0	-11.437	2.542	0.0
0.0	0.0	0.0	0.0	0.0	4.153

$ABD^{RSE} - ABD^{CLT}$

-823.9	-191.6	17.5	210.7	-129.1	14.5
-191.6	-789.4	17.1	-164.1	386.4	13.9
17.5	17.1	36.2	16.4	14.7	65.1
210.7	-164.1	16.4	557.7	-114.7	17.1
-129.1	386.4	14.7	-114.7	509.8	16.0
14.5	13.9	65.1	17.1	16.0	75.7

Fig. 16. Relative (left) and absolute (right) influence of the large fuzzball on the stiffness of the RSE.

defect size is not easily defined. The inferred stiffness degradations of elements used in macroscale simulations must therefore take the RSE size into account.

4. Conclusion

The physical mesoscale modelling approach presented in this paper provides a promising foundation for the analysis of the mechanical impact of AFP-specific manufacturing-induced defects in CFRP structures. The RSE model provides a numerical tool to build an extensive database of the mechanical influence of parameterised, structurally complex defects within composites. Such databases are invaluable for the decision-making of which defects need removal during AFP layup. The possibility to accurately assess the effects of fuzzballs is a novelty in this research area. The presented RSE approach allows for a general evaluation of material segments, comparable to a typical representative volume element. Additionally, the increased size of the modelling volume also allows for an investigation of a variety of other AFP-induced defects in high detail, such as gaps, overlaps, tow-twists or other foreign objects. The quality of the results is highly dependant on the assumptions and simplifications of the detailed model. When using the presented RSE approach for researching the effects of defects, the main difficulty is the determination of a suitable sizing of the RSE in comparison to the defect itself, as this ratio has a significant influence on the actual values of the computed stiffnesses of the RSE. This is especially true for defects leading to a relative displacement between the composite layers, which is not accounted for in the presented approach due to the requested comparability of the RSE outcome to the classical lamination theory. If the results are to be incorporated into a higher-level multiscale model, the authors expect that choosing the actual size of the element containing the defect as the size of the RSE will lead to good results.

To further improve the RSE approach, the simulation results need to be compared to experimental tests in follow-up research. Compression tests have been carried out by the authors in [34], as the RSE response of fuzzballs indicates a positive impact on the buckling behaviour of the composite structure. The RSE approach should be extended with modelling techniques to accurately evaluate the failure modes of the composite constituents. Following the multiscale approach, the use of microscale simulations might be feasible for obtaining averaged material characteristics, such as for the fuzzball material.

An additional improvement would be the determination of the strength and the non-linear behaviour before failure of the RSE to derive a general stress-strain curve comparable to a typical material characterisation. This would require the possibility to group (geometrically) similar defects that also exhibit a similar strength and failure behaviour, to be usable in a general application.

Lastly, the RSE approach presented in this paper allows for an in-situ assessment of AFP-induced defects by forwarding process monitoring data to simulations. However, the geometry of a defect changes during curing, thus necessitating further research into the influence of autoclave curing on defect deformation. From a practical perspective, it might prove difficult to capture the geometry of defects in the necessary detail during industrial layup. Although non-destructive testing methods for detecting defects in composite parts post curing exist, these generally do not provide the geometric detail needed for the presented RSE approach.

Declaration of Competing Interest

The authors declare that they have no known competing financial interests or personal relationships that could have appeared to influence the work reported in this paper.

Data availability

Data will be made available on request.

References

[1] F. Heinecke, C. Willberg, Manufacturing-induced imperfections in composite parts manufactured via automated fiber placement, J. Compos. Sci. 3 (2019) 56, https://doi.org/10.3390/jcs3020056.

[2] D.H.-.J.A. Lukaszewicz, C. Ward, K.D. Potter, The engineering aspects of automated prepreg layup: history, present and future, Compos. Part B: Eng. 43 (2012) 997–1009, https://doi.org/10.1016/j.compositesb.2011.12.003.

[3] D. Maass, Progress in automated ply inspection of AFP layups, Reinforced Plastics 59 (2015) 242–245, https://doi.org/10.1016/j.repl.2015.05.002.

[4] F. Heinecke, T. Wille, In-situ structural evaluation during the fibre deposition process of composite manufacturing, CEAS Aeronaut J. 9 (2018) 123–133, https://doi.org/10.1007/s13272-018-0284-5.

[5] S. Sun, Z. Han, H. Fu, H. Jin, J.S. Dhupia, Y. Wang, Defect characteristics and online detection techniques during manufacturing of FRPs using automated fiber placement: a review, Polymers (Basel) 12 (2020) 1337, https://doi.org/10.3390/polym12061337.

[6] B. Denkena, C. Schmidt, K. Völtzer, T. Hocke, Thermographic online monitoring system for automated fiber placement processes, Compos. Part B: Eng. 97 (2016) 239–243, https://doi.org/10.1016/j.compositesb.2016.04.076.

[7] B. Denkena, C. Schmidt, M. Timmermann, A. Friedel, An optical-flow-based monitoring method for measuring translational motion in infrared-thermographic images of AFP processes, Prod. Eng. Res. Devel (2021) https://doi.org/10.1007/s11740-021-01084-w.

[8] C. Schmidt, B. Denkena, K. Völtzer, T. Hocke, Thermal image-based monitoring for the automated fiber placement process, Procedia CIRP 62 (2017) 27–32, https://doi.org/10.1016/j.procir.2016.06.058.

[9] C. Schmidt, T. Hocke, B. Denkena, Deep learning-based classification of production defects in automated-fiber-placement processes, Prod. Eng. Res. Devel. 13 (2019) 501–509, https://doi.org/10.1007/s11740-019-00893-4.

[10] X. Li, S.R. Hallett, M.R. Wisnom, Modelling the effect of gaps and overlaps in automated fibre placement (AFP)-manufactured laminates, Sci. Eng. Compos. Mater. 22 (2015) 115–129, https://doi.org/10.1515/secm-2013-0322.

[11] M. Lan, D. Cartié, P. Davies, C. Baley, Microstructure and tensile properties of carbon–epoxy laminates produced by automated fibre placement: influence of a caul plate on the effects of gap and overlap embedded defects, Compos. Part A: Appl. Sci. Manuf. 78 (2015) 124–134, https://doi.org/10.1016/j.compositesa.2015.07.023.

[12] W. Woigk, S.R. Hallett, M.I. Jones, M. Kuhtz, A. Hornig, M. Gude, Experimental investigation of the effect of defects in automated fibre placement produced composite laminates, Compos. Struct. 201 (2018) 1004–1017, https://doi.org/10.1016/j.compstruct.2018.06.078.

[13] A. Sawicki, P. Minguett, The effect of intraply overlaps and gaps upon the compression strength of composite laminates, in: 39th AIAA/ASME/ASCE/AHS/ASC Structures, Structural Dynamics, and Materials Conference and Exhibit, American Institute of Aeronautics and Astronautics, Long Beach, CA, U.S.A., 1998, https://doi.org/10.2514/6.1998-1786.

[14] K. Fayazbakhsh, M. Arian Nik, D. Pasini, L Lessard, Defect layer method to capture effect of gaps and overlaps in variable stiffness laminates made by Automated Fiber Placement, Compos. Struct. 97 (2013) 245–251, https://doi.org/10.1016/j.compstruct.2012.10.031.

[15] K. Croft, L. Lessard, D. Pasini, M. Hojjati, J. Chen, A. Yousefpour, Experimental study of the effect of automated fiber placement induced defects on performance of composite laminates, Compos. Part A: Appl. Sci. Manuf. 42 (2011) 484–491, https://doi.org/10.1016/j.compositesa.2011.01.007.

[16] G. Seon, Y. Nikishkov, A. Makeev, Structures perspective for strength and fatigue prognosis in composites with manufacturing irregularities, J. Am. Helicopter Soc. 60 (2015) 1–10, https://doi.org/10.4050/JAHS.60.011002.

[17] F. Heinecke, W. van den Brink, T. Wille, Assessing the Structural Response of Automated Fibre Placement Composite Structures With Gaps and Overlaps By Means of Numerical approaches, Kopenhagen, 2015, p. 13.

[18] B. El Said, S.R. Hallett, Multiscale surrogate modelling of the elastic response of thick composite structures with embedded defects and features, Compos. Struct. 200 (2018) 781–798, https://doi.org/10.1016/j.compstruct.2018.05.078.

[19] A. Hannig, P. Horst, B. Fiedler, Static and Fatigue Transverse Crack Initiation in Thin-Ply Fibre-Reinforced Composites, TU Braunschweig, Niedersächsisches Forschungszentrum für Luftfahrt, 2018.

[20] A. Schmitz, P. Horst, A finite element unit-cell method for homogenised mechanical properties of heterogeneous plates, Compos. Part A: Appl. Sci. Manuf. 61 (2014) 23–32, https://doi.org/10.1016/j.compositesa.2014.01.014.

[21] A. Schmitz, P. Horst, Numerical Modelling of the Change in Stiffness Properties of Cross-Ply Laminates Subjected to Large Bending Curvatures, KEM, 2013, pp. 577–578, https://doi.org/10.4028/www.scientific.net/KEM.577-578.173, 173–6.

[22] H. Schürmann, Konstruieren Mit Faser-Kunststoff-Verbunden. 2., bearb. Und erw. Aufl, Springer, Berlin, 2007.

[23] R.M. Jones, Mechanics of Composite Materials, 2. ed, Taylor & Francis, Philadelphia, 1999.

[24] J.N. Reddy, Theory and Analysis of Elastic Plates and Shells, 2. ed, CRC Press, Boca Raton, Fla, 2007.

[25] VDI 2014-3:2006, Kunststofftechnik - Entwicklung Von Bauteilen Aus Faser-Kunststoff-Verbund: Berechnungen, Beuth Verlag GmbH, 2006.

[26] A. Kaddour, M. Hinton, P. Smith, S. Li, Mechanical properties and details of composite laminates for the test cases used in the third world-wide failure exercise, J. Compos. Mater. 47 (2013) 2427–2442, https://doi.org/10.1177/0021998313499477.

[27] A.O. Cifuentes, A. Kalbag, A performance study of tetrahedral and hexahedral elements in 3-D finite element structural analysis, Finite Elements in Anal. Design 12 (1992) 313–318, https://doi.org/10.1016/0168-874X(92)90040-J.

[28] K.M. Engel, P. Horst, D. Meiners, Technische Universität Braunschweig, Berücksichtigung prozessinduzierter Effekte in der Auslegung von Faser-Kunststoff-Verbunden, 2018.

[29] K.M. Engel, P. Horst, T. Hundt, C. Schmidt, B. Denkena, Effect of Manufacturing Process Induced Fiber Waviness On Mechanical Properties of Composite Structures By Example of a Prepreg Forming process, Seville, Spain, 2014.

[30] Ric J.P.-.H. Belnoue, M.A. Valverde, M. Onoufriou, X. Sun, D.S. Ivanov, S. R. Hallett, On the physical relevance of power law-based equations to describe the compaction behaviour of resin infused fibrous materials, Int. J. Mech. Sci. (2021) 106425, https://doi.org/10.1016/j.ijmecsci.2021.106425.

[31] B. Denkena, C. Schmidt, P. Weber, Automated fiber placement head for manufacturing of innovative aerospace stiffening structures, Procedia Manuf. 6 (2016) 96–104, https://doi.org/10.1016/j.promfg.2016.11.013.

[32] Hexcel, HexPly 8552 Epoxy Matrix (180°C/356°F Curing Matrix): Product Data Sheet, editor, 2016.

[33] Object Research Systems (ORS) Inc, Dragonfly, 2021. http://www.theobjects.com/dragonfly.

[34] A. Friedel, S. Heimbs, P. Horst, C. Schmidt, M. Timmermann, F. Hakiri, et al., in: Impact of automated fibre placement induced defects on the compression behaviour of CFRP structures, 2022.

[35] X. Lu, M. Ridha, B.Y. Chen, V.B.C. Tan, T.E. Tay, On cohesive element parameters and delamination modelling, Eng. Fract. Mech. 206 (2019) 278–296, https://doi.org/10.1016/j.engfracmech.2018.12.009.

[36] H.M. Deuschle, 3D Failure Analysis of UD Fibre Reinforced composites: Puck's theory Within FEA, Inst. für Statik und Dynamik der Luft- und Raumfahrtkonstruktionen, Stuttgart, 2010.